Large Eddy Simulations of complex multicomponent swirling spray flames in a realistic gas turbine combustor

Varun Shastry[a,*], Eleonore Riber[a], Laurent Gicquel[a], Bénédicte Cuenot[a], Virginel Bodoc[b]

[a] *CERFACS, 42 Avenue Gaspard Coriolis, Toulouse Cedex 1, 31057, France*
[b] *ONERA/DMPE, 2 Avenue Edouard Belin, Toulouse, 31055, France*
*Corresponding author, Email address: varun.shastry@cerfacs.fr

Abstract

Large Eddy Simulations of the realistic liquid fueled gas turbine combustor LOTAR operated at ONERA are performed for two fuels; a conventional JetA-1 and an alternative alcohol to jet fuel At-J, each modeled by a 3-component formulation. JetA-1 is composed of n-dodecane, methyl-cyclohexane and xylene each corresponding to the major hydrocarbon families found in real fuel. At-J is a synthetic drop in fuel composed of only branched chain alkanes, iso-octane, iso-dodecane and iso-hexadecane. Analytically reduced chemistry and multicomponent spray evaporation model coupled to the dynamic thickened flame turbulent combustion model are employed to understand the processes involved in turbulent spray flames in the LOTAR configuration. The objectives are to predict and understand the potential effects of staged vapourisation and consumption of the fuel components, and their impact on the spray flame structures. Simulations confirm the role of preferential evaporation in establishing and stabilising the reaction zone. JetA-1 evaporation zones extend deep into the rich burnt gasses resulting in a combustion regime with the possibility of droplet clusters burning individually. At-J which is more volatile, leads to complete combustion with the majority occurring due to the premixed lean reactions of the smaller pyrolysed components. The need to further include models capable of identifying and handling combustion regimes encountered in such spray flames is hence highlighted. This work is intended as a starting point for improving multicomponent spray modelling and requires additional experimental data for validation.

Keywords: Large Eddy Simulation; Spray flames; Analytically reduced chemistry; Multicomponent evaporation; Sustainable Aviation Fuel

Submitted to: **Colloquium 14: cc/ccc use only**

1. Introduction

Detailed modelling and simulation techniques are an invaluable tool complementing other design strategies to understand the various sub-processes occurring in combustion systems. At present, the state-of-the-art gas turbine combustors use complex liquid injection and combustion strategies for efficient energy conversion [1]. Simultaneous occurrence of mechanisms over multiple length and time scales which include gaseous and droplet combustion are widely reported in literature [2]. Simulations of various scales of configurations have successfully captured these multiple combustion regimes present in spray flames [3–6].

Commercial fuels contain hundreds of components belonging to multiple families of hydrocarbons [7], each with their own combustion and vapourisation characteristics. Further with the push towards Sustainable Aviation Fuels (SAFs) in the transition to net zero emissions, additional components are being introduced to the already existing pallet [8]. SAFs refers to renewable hydrocarbons produced from a range of sustainable raw materials whose properties match the standard aviation fuels. These can then be blended with traditional fossil fuels or be utilised directly in existing infrastructure earning them the name "drop-in" fuels. Developing models and simulations methodologies to understand the combustion of multicomponent Jet fuel, SAF and their blends in existing gas turbine architecture is therefore the first step towards such a successful transition.

Literature on swirled multicomponent spray flame simulations of jet fuels is limited [9, 10]. The detailed study by [10] of a lab scale burner with a multicomponent fuel representation indicate the rate controlling effects of preferential evaporation and highlight its advantages in the pollutant predictions. The approach used was to couple a Continuous Multicomponent Model (CMC) with detailed chemistry. CMC approach requires accurate fuel composition data which may not be always available, and in their work each fuel group ultimately collapses to a discrete representation in the gas phase reactive calculations. Additionally, the flame was fully resolved with a fine mesh, which while being accurate makes it impractical for applications towards large scale industrial configurations.

The standard validated approach of using Large Eddy Simulation (LES) with a Dynamically Thickened Flame (DTF) model is extended in the present work by coupling it with a Discrete Multicomponent (DMC) evaporation model. In the DTF-LES, the reactive front is scaled by a factor $\mathcal{F}$ so as to be able to track it on a relatively coarse grid. The scaling is applied only in regions where a flame is detected by the sensor $\mathcal{S}$. The flame front $\mathcal{S}$ is identified by the progress of the fuel-oxidation reaction (global chemistry) or fuel consumption rate (multi-step chemistry) [11], and in its original formulation needs calibration using pre-computed 1D laminar flames. In case of two phase flames the constantly varying equivalence ratio, composition and liquid loading makes the calibration space difficult to be pre-defined. To overcome these issues a generic flame sensor based on purely geometric considerations and no pre-calibration has been utilised here [12].

The first objective of the work is combining state of the art modelling approaches to simulate multicomponent spray flames on a large scale configuration. The "Liquid fueled Onera Thermo-Acoustic Rig" (LOTAR) setup chosen for this work is unique due to its proximity in complexity to a realistic industrial case [13]. The major parameters of the configuration are shown in Table. 1. The second objective is understanding the effects of fuel composition by comparing the swirled spray flames of standard jet fuel (JetA-1) and an alternative alcohol to jet fuel (At-J) in the LOTAR configuration under identical operating conditions. The differences in spray flame structures, observed regimes and the influence of preferential evaporation are highlighted.

Parameter	**Value**
Reynolds number	$\mathbf{O}\left(10^6\right)$
Density ratio	$\mathbf{O}\left(10^6\right)$
Stokes number	$3-13$
Thermal power	$200\,\mathrm{kW}$

Table 1: Major parameters of the LOTAR configuration comparable to an industrial case [14].

2. Numerical Setup and modelling

Details of the experimental setup are available in literature, which primarily focussed on self sustained instabilities [13]. The computational domain of interest shown in Fig. 1a is the water-cooled combustion system $0.515\,\mathrm{m}$ long, separated into an upstream plenum and a downstream chamber ($0.12\,\mathrm{m} \times 0.12\,\mathrm{m}$ cross section) separated by a specially designed fuel injector and perforated plate. The injection system (Fig. 1b) consists of two counter rotating axial swirlers to break up the central pilot jet. This is surrounded by a radial swirler through which bulk of the injected air passes. Additionally, 6 multipoint injectors are present in the radial swirler. The unstructured mesh used for the LES is composed of 32 million tetrahedrons with a refined swirler region shown in Fig. 1c. The smallest mesh size of about 0.2 mm is used in the injector region.

Cold flow simulations done at 1 bar, $T_{air} = 298\,\mathrm{K}$ and $\dot{m}_{air} = 100\,\mathrm{g/s}$ were used to validate the numerical approach. The reactive simulations are targeted to study the set of experiments performed at a pressure of 1 bar and an over lean global equivalence ratio of around 0.6 . For both the reactive cases discussed, the inlet air mass flow rate is $\dot{m}_{air} = 100\,\mathrm{g/s}$ at a temperature $T_{air} = 450\,\mathrm{K}$. The corresponding liquid fuel injection rate is $\dot{m}_{liq} = 4.55\,\mathrm{g/s}$ at liquid injection temperature $T_{liq} = 298\,\mathrm{K}$.

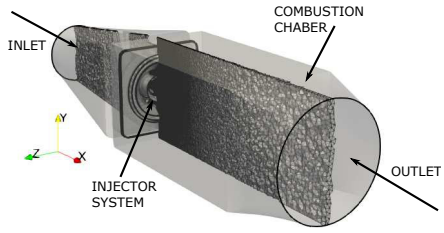

(a) Computational domain.

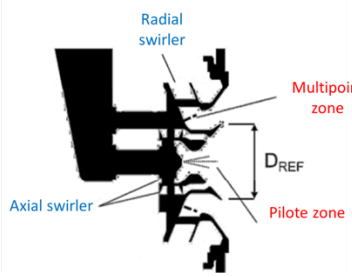

(b) Swirler and injection system [13].

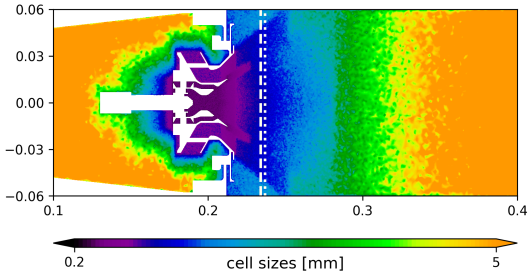

(c) Mesh sizes and sections at $x = 22mm$ (dashed) and $x = 25mm$ (dotted).

Fig. 1: Computational details of the setup.

The simulations have been performed using the 3-D fully compressible reactive flow solver AVBP [15]. The second-order accurate Lax-Wendroff convective scheme [16] is used with an explicit Runge-Kutta time stepping. The subgrid-scale closure for turbulence is addressed using the SIGMA model [17]. The flame is thickened on 5 mesh points with an efficiency function to account for the subgrid-scale turbulent interactions [18]. The flame front is detected using a generic self-adapting sensor based on purely geometric considerations, and is identified by concave shape of the chemical activity (heat release) with the complete details and implementation given in [12]. A constant heat flux of $-75000.0\,\mathrm{Jm^{-2}s^{-1}}$ is imposed on the chamber walls based on experimental measurements.

The liquid phase is modelled using the Lagrangian point particle approach and the particle evolution is tracked in the Eulerian gas phase. The evaporation is modelled according to the Abramzon-Sirignano model considering infinite conductivity, mass diffusivity inside the droplet [19]. The source terms for mass, momentum and energy from the liquid phase are distributed to the nearest nodes in the Eulerian gas phase to handle the two-phase coupling. The readers are referred to the prior works [6, 20] for the further details and validation of the liquid phase modelling on multiple configurations.

The liquid injection profile is chosen considering a fuel split ratio (FSP) of 100%, i.e., all the fuel is injected through the pilot injector. A hollow cone spray is modelled using the semi-empirical FIM-UR model [21] and a Rosin-Rammler droplet diameter distribution having a Sauter Mean Diameter (SMD) of 30 μm and a shape parameter q=1.7 is injected. Droplets impacting the inner walls of the injection system form a liquid film. A separate film atomisation model has not been included in the present study.

Two fuel compositions each having 3 components are considered. JetA-1 surrogate consists of n-dodecane (NC12H26), methyl-cyclohexane (MCYC6) and xylene (XYLENE) representing three common families of hydrocarbons found in commercial fuels, i.e., straight chain alkanes, cycloalkanes and aromatics respectively. JetA-1 surrogate has an average molar mass of 142.8 g/mol and a H/C ratio of 2.0. An alternative to the petroleum based JetA-1, Alcohol-to-Jet Synthetic Paraffinic Kerosene (AtJ-SPK) is produced from pathways where sugars and starches are fermented and processed. At-J is composed of only branched chain hydrocarbons iso-octane (IC8H18), iso-dodecane (IC12H26) and iso-hexadecane (IC16H34). The average molar mass and H/C ratio of At-J is 170 g/mol and 2.17 respectively. Further details about the fuels, their properties and experimental data on gas turbine engines have been reported in literature [22]. The volatilities of the fuel components in terms of the normal boiling point is given in Table. 2 which indicate that MCYC6 and IC8H18 are the most volatile components of the JetA-1 and At-J respectively.

The corresponding Analytically Reduced Chemistry (ARC) schemes have been derived using the code ARCANE [23]. The major details of the ARC are given in Table. 2 and provided as supplementary material.

	NC12H26	MCYC6	XYLENE
Mole fraction (X)	0.6	0.2	0.2
Normal Boiling Point	489.48 K	374.09 K	413.82 K
	Transported Species	QSS species	Reactions
ARC	36	16	543

(a) JetA-1 composition and ARC **A1_36_543_16_QC**.

	IC8H18	IC12H26	IC16H34
Mole fraction (X)	0.08	0.84	0.08
Normal Boiling Point	372.45 K	450.95 K	513.2 K
	Transported Species	QSS species	Reactions
ARC	31	24	394

(b) At-J composition and ARC **B1_31_394_24_JW**.

Table 2: Details of multicomponent fuel composition and ARC.

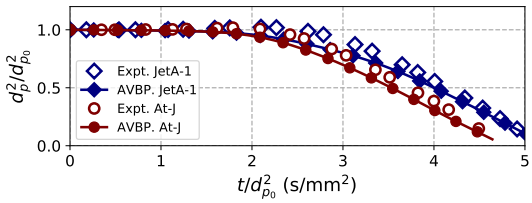

(a) Evolution of the normalised diameter [24].

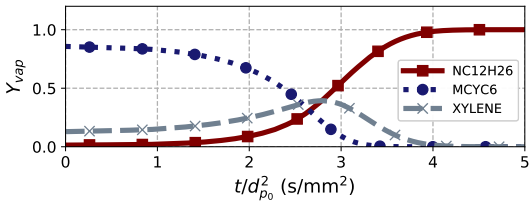

(b) Vapour flux composition for JetA-1.

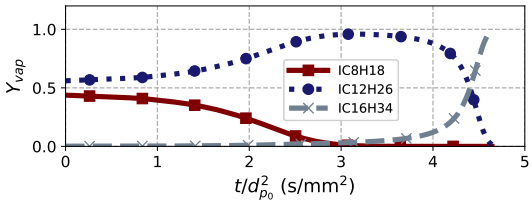

(c) Vapour flux composition for At-J.

Fig. 2: Evaporation and vapour flux composition data for a freely falling droplet validating the multicomponent evaporation model and fuel.

The Abramzon-Srignano [19] evaporation model has been extended to the multicomponent fuels by considering the phase change of each individual component. The resulting model termed the discrete multicomponent model (DMC) has been validated previously and used to study the propagation of laminar spray flames of JetA-1 [25]. For the present study, validations against experimental data of a freely falling droplet [24] are shown in Fig. 2. Though JetA-1 is lighter in comparison to At-J, a negative correlation of the mean liquid molar mass and the evaporation rate is observed in Fig. 2, with At-J evaporating 15% faster than JetA-1.

A feature of evaporation of real fuels is the constantly varying evaporation flux through the droplet lifetime. The most volatile components evaporate first, followed by the heavier components which can be observed for both cases in Fig. 2. In addition to the different evaporation rates, the evolution of the vapor flux composition shows completely different behaviors due the varying concentrations of liquid species present in each fuel (Table. 2).

Since At-J has a single dominant species IC12H26 (X = 84 %), its effect on the vapor composition is clearly reflected with contribution from the volatile IC8H18 only present in the initial stages (Fig. 2, bottom) and negligible contribution from the heavy IC16H34 until close to the end. In the vapor flux composition of JetA-1 (Fig. 2, middle), two stages can be identified where for the first quarter of the droplet lifetime, the volatile MCYC6 dominates, with the final half consisting only of NC12H26.

The DMC model can be easily integrated with ARC for two phase reactive calculations. The preferential vapourisation trends shown in Fig. 2 can give rise to an inhomogeneous and stratified mixture composition over the combustor domain as the spray evolves. This effect is enhanced in the presence of evaporating droplets entering a flame front [25] and the ARC must be valid over a wide range of mixture compositions. The ternary plots in Fig. 3 show the sensitivity of the ARC to the possible changes in composition space by plotting the laminar flame speeds at stoichiometry. The variations are moderate and similar trends are seen for both rich and lean mixtures (not shown) indicating that the chemical scheme handles all possible effects of preferential evaporation and mixing. JetA-1 shows a larger variation with lower speeds in regions dominated by XYLENE while At-J has a lesser flame speed variation due to its composition dominated by IC12H26.

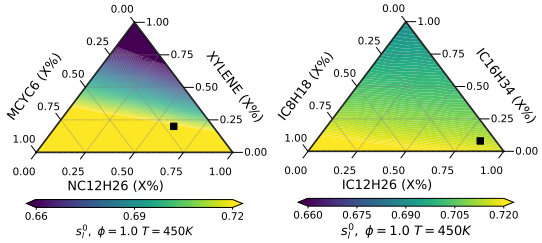

(a) JetA-1. **(b)** At-J.

Fig. 3: Flame speed variation across range of compositions. Black pointer indicates liquid composition given in Table. 2.

3. Results

3.1. Validation of the numerical setup

A comparison with experimental data for gas and droplet statistics for JetA-1 is shown in Fig. 4. The axial gas velocities are measured at cold flow conditions and the droplet statistics are obtained in a reacting environment. The sections where measurements are made is shown in Fig. 1c. The presence of a large fuel injection stem in the inlet plenum, causes an asymmetry in the axial gas velocity profiles with a maximum of 50 $^{m}/_{s}$ in the lower branch and 30 $^{m}/_{s}$ in the upper one. This difference and opening of the jet is well captured by the simulations across both sections, seen in Fig. 4a.

The profiles obtained for the average droplet diameters (d10) and the axial velocity match the trends observed in the experimental data, seen in Fig. 4b. Large droplets are present in the central recirculation zone (CRZ) and their sizes are underestimated by 10%,

which lead to a slightly narrower spray opening angle in the chamber. The injected values of the droplet diameter distribution is slightly smaller than ones in the experiments (data made available after starting the simulations), therefore the particles relax fast to the gas velocity, finally leading to a slight over prediction of the droplet velocity and spray angle. Overall, the setup captures the major features measured in the experiments and due to the FSP=100% operating conditions chosen for the simulations, the differences do not alter the global flame shapes and structures discussed hereafter.

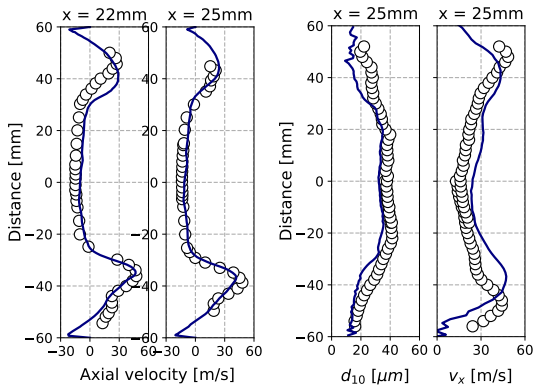

(a) Gas axial velocities. **(b)** Droplet statistics.

Fig. 4: Comparison of the cold flow LES (solid line) gas and reacting flow droplet properties with experimental data (symbols) at various axial locations.

3.2. Global evaporation, heat release trends

The differences in composition of the two fuels have a significant effect on the overall evaporation zones, leading to different flame structures and regimes. In Fig. 5, the total evaporation fluxes in the mid-plane averaged over 6 ms is shown for JetA-1 and At-J respectively.

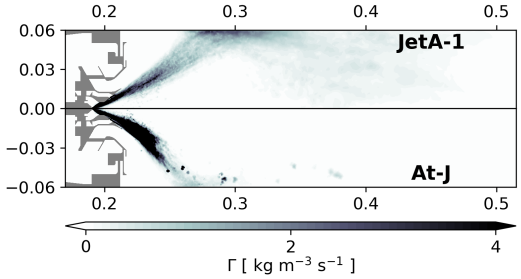

Fig. 5: Comparison of the time-averaged field of total evaporation rate in the midplane for both fuels.

JetA-1 having a longer vapourisation timescale (Fig. 2, top), is present deep into the combustion chamber, peaking in the region around $x = 0.24\,\mathrm{m}$. A weaker zone in the burnt gasses is also observed post $x = 0.3\,\mathrm{m}$. NC12H26 being the heaviest component which remains in the liquid fuel, contributes completely to the total evaporation in this downstream region. Contrarily, At-J with a faster vapourisation timescale completely evaporates over a shorter distance with negligible evaporation rate beyond $x = 0.24\,\mathrm{m}$ (Fig. 2, bottom). The dominant species IC12H26 (84%) closely follows the complete evaporation trends across the chamber. Large droplets do not reach the downstream regions as observed in the case of JetA-1.

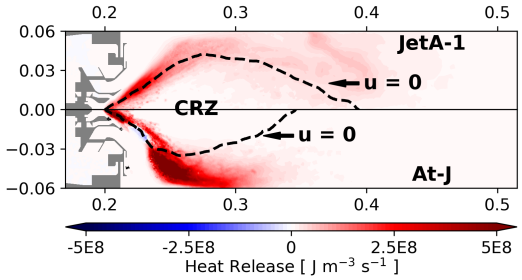

Fig. 6: Comparison of the time-averaged field of heat release rate in the midplane for both fuels.

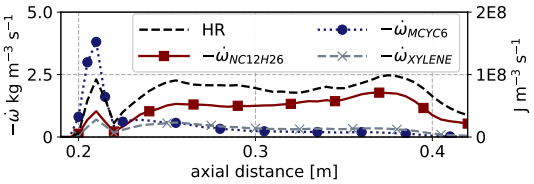

(a) JetA-1

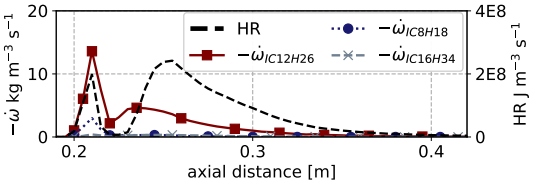

(b) At-J

Fig. 7: Cross sectional average consumption rates of the fuel components along the chamber.

The time-averaged fields of Heat Release (HR) rates for JetA-1 and At-J are shown in Fig. 6. The swirl induced on the incoming flow results in the formation of a large CRZ containing hot combustion products. This CRZ serves the dual purpose of both stabilizing the flame and promoting quick evaporation and mixing of the injected liquid fuel to sustain the flame. The CRZ is identified as the region bounded by the black dashed lines of zero axial velocity. The flame base for both cases lies inside the injector at $x = 0.2\,\mathrm{m}$ along the marked CRZ highlighting this stabilizing mechanism.

Also plotted in Fig. 7 are the cross sectional average consumption rates of each fuel component and the heat release along the combustion chamber axis. For both fuels two regions of peak heat release can be observed. The first peak around $x = 0.2\,\mathrm{m}$ is due the reactions in the injector where the flame stabilisation and initialisation occur. For JetA-1 this HR peak coincides with the consumption of MCYC6. For At-J, the initial increase in heat release is associated with the evaporation and consumption of IC12H26, the dominant fuel component.

Further downstream the heat release patterns for the fuels show a considerable change. As seen previously, the evaporation zone of JetA-1 continues further in the domain. Inside these high temperature regions, the evaporation, consumption and heat release patterns follow each other indicating significant contribution of the heavier NC12H26 to the reactions inside the combustion chamber. For At-J, the secondary heat release peak follows the consumption profiles of IC12H26 with a spatial delay, and shows complete combustion before the chamber exit.

3.3. Flame structures for JetA-1

Instantaneous snapshots of heat release displayed in Fig. 8 clearly mark the three observed separate features. **Region I**, extending from the flame base in the injector bowl into the chamber is a continuous reactive zone, where the evaporated components mix with the incoming air and are consumed. A part of this continuous reaction zone is dominated by MCYC6 inside the injector and NC12H26 in the combustion chamber.

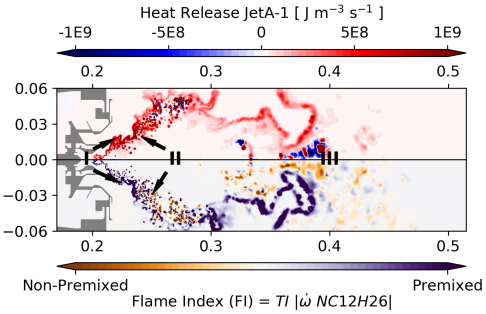

Fig. 8: Instantaneous heat release rate field (top) and Flame Index (botttom) for JetA-1.

A visual representation of this is presented by plotting the evaporation and consumption of MCYC6 in Fig. 9. High vapourisation rates inside the injector mainly correspond to the preferential release of the volatile MCYC6 vapour. The weaker evaporation zone of MCYC6 observed inside the chamber is due to the larger droplets and enhanced evaporation in the unsaturated regions further downstream. This MCYC6 vapour mixes with the fresh incoming gases and its consumption region overlaps with the high heat release rate region observed in Fig. 7, indicating the role of volatile components in flame stabilization. NC12H26 vapour is released in the latter stages of the droplet lifetime. This evaporation and consumption are responsible for the latter half of **Region I** inside the chamber. These zones of evaporation and consumption of NC12H26 are shown in Fig. 10.

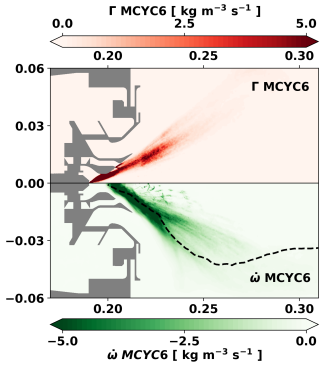

Fig. 9: Time-averaged evaporation (top) and consumption (bottom) zones of MCYC6.

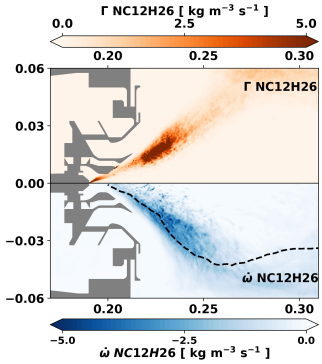

Fig. 10: Time-averaged evaporation (top) and consumption (bottom) zones of NC12H26.

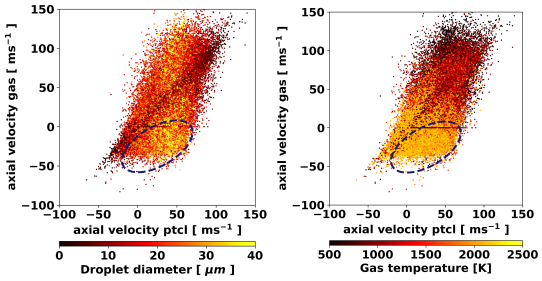

Fig. 11: Scatter plot of particle and gas axial velocities coloured by droplet diameter (left) and gas temperature (right).

A wide turbulent flame brush with two regions of fuel combustion can be observed, delineated approximately by the recirculation zone, with the inner zone

marked as **Region II**. Large droplets with ballistic trajectories cross **Region I** and enter the CRZ. These are visualised through the scatter plots of the droplet and gas axial velocities projected at the particle locations in Fig. 11. The droplets that enter the recirculation zone are associated with regions of negative axial gas velocity and high temperature, marked by the blue dashed ellipse. The high relative velocity and high temperature promote rapid evaporation of these droplets. This quick phase change, immediate consumption and heat release in the rich regions appear as the discrete spots, marked as **Region II** in Fig. 8.

Further downstream in regions of low droplet density one observes a reaction zone with multiple combustion modes marked as **Region III**. The vapour-air mixture is diluted by the burnt gases here which manifests as an extension of the continuous reaction zone. The large droplets which reach the high temperature downstream zones burn individually. Such behaviour was already observed in earlier studies [6] and indicates the need for isolated droplet burning models to be incorporated in such simulations. Since the evaporation zone is extending towards the combustor exit and the vapour flux is mainly NC12H26, it leads to the possibility of incomplete combustion.

The combustion regime can be analysed using the Normalised Takeno Index (TI) defined using the mass fraction Y as:

$$TI = \frac{\boldsymbol{\nabla} Y_F \boldsymbol{\nabla} Y_{Ox}}{|\boldsymbol{\nabla} Y_F| . |\boldsymbol{\nabla} Y_{Ox}|} \tag{1}$$

Opposing gradients leading to $TI = -1$ are an indication of non-premixed combustion while premixed zones have $TI = +1$. The presence of multiple combustible species necessitates an altered definition of Eq. 1 [20]. For the present work, the index is reconstructed for post priori analysis using $Y_F = Y_{NC12H26} + Y_{MCYC6} + Y_{XYLENE}$. The TI is then conditioned using the $\dot{\omega}_{NC12H26}$ to get the flame index (FI) as $FI = TI\ |\dot{\omega}_{NC12H26}|$, and used to see individual flame regimes. This makes sense because it is the dominant component in the liquid fuel and its presence throughout the reactive zone from point of injection to the downstream regions was seen previously. FI for JetA-1 fuel is plotted in Fig. 8. The **Region I** is seen as a premixed region, where the highly turbulent flow from the radial swirlers enhance the mixing resulting in a wrinkled flame. In **Region II** and **Region III**, where droplet groups are more probable to burn as individual particles or small localised clusters, non premixed combustion modes are prominent. Such behaviours were also observed in the multicomponent simulations using a similar fuel composition [10], in the near wall regions where hot gasses were trapped. It is not possible to resolve the flame around a droplet in a Lagrangian point particle setup as mesh sizes are of the same order as the fuel droplets. The challenges in modelling such a combustion regime lies in identifying regions where the inter-droplet spacing S_d is more than the diameter of the flame d_f around a single burning droplet. This is then followed by identifying the correct time-scale for the auto-ignition [26]. Additionally, in case of a multicomponent droplet one needs to account for the changing evaporation flux Fig. 2 and the source terms to the gas phase.

3.4. Flame structures for At-J

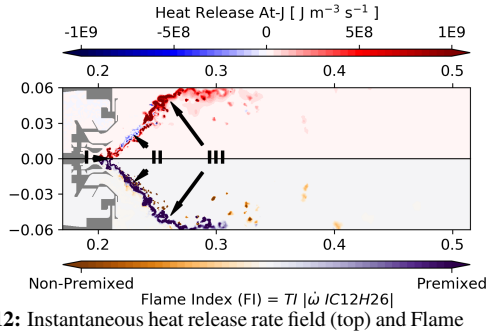

Fig. 12: Instantaneous heat release rate field (top) and Flame Index (bottom) for At-J.

For At-J, an instantaneous snapshot of the heat release identifying three distinct zones are shown in Fig. 12. **Region I** is the flame base inside the injector, where the premixed combustion of the volatile species with the incoming air initiates the flame. This is similar to the previous JetA-1 case, however along with IC8H18 (most volatile), the dominant IC12H26 is also playing a role in flame stabilization (averaged consumption rates not shown).

Similar to the case with JetA-1, the TI in this case is constructed using $Y_F = Y_{IC12H26} + Y_{IC8H18} + Y_{IC16H34}$ in Eq. 1. The FI for At-J obtained by conditioning the TI with $\dot{\omega}_{IC12H26}$ as $FI = TI\ |\dot{\omega}_{IC12H26}|$ is visualised in Fig. 12. The choice of IC12H26 is straightforward because of the At-J composition. The entire reaction zone can be characterised as a continuous premixed flame. Individual droplet combustion regions appearing as spots are insignificant compared to JetA-1 and are observed mainly in the downstream region where the occasional large droplets exist. Due to the quick evaporation, the number of ballistic droplets that cross over into the recirculation zones are reduced.

The evaporation zone ends at the point $x = 0.24\,\mathrm{m}$ and results in a concentration of fuel vapour just above the injector exit. This overlaps with a region having discernible negative heat release marked **Region II** that can be observed in both the instantaneous and time-averaged fields. This pool of vapour comes in contact with the hot recirculation gasses and undergoes dissociation into smaller components which explains the negative heat release that is observed. As an example two of the smallest pyrolysis components C_2H_2 and CH_4 are visualised in Fig. 13 by the solid iso-contour corresponding to $Y = 0.01$ and coinciding with **Region II**. Here, some of these components react with the rich recirculation zone as seen by

a thin heat release region. Also a weak zone of non-premixed reactions can be observed in Fig. 12 towards swirler exit, which however is very insignificant.

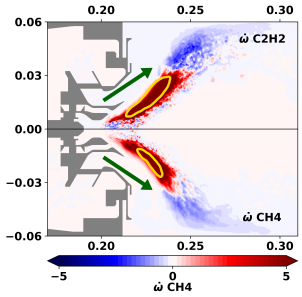

Fig. 13: Time averaged fields in the mid plane of the production and consumption rates of pyrolysed components.

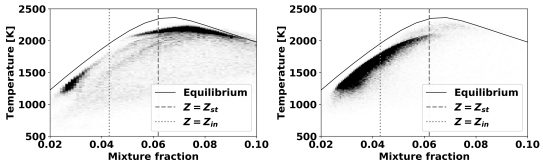

(a) Region II. **(b)** Region III.

Fig. 14: Probability density plots in the temperature- mixture fraction space for the At-J flame.

A probability map of **Region II** is shown in Fig. 14a with the dark regions indicating higher probabilities. The dashed and dotted lines represent the stoichiometric and global inlet conditions respectively. It is very clear that increasing fuel concentration due to quick evaporation of the At-J followed by its dissociation increases the local equivalence ratio leading to a rich reactive zone.

The incoming fresh gases from the radial swirlers (green arrows Fig. 13) under turbulent conditions promote quick mixing and ignition of the smaller pyrolysis components. This mixture ignites further downstream in **Region III** causing the sudden increase in the thickness of the reaction zone and intense heat release rate. This also explains the delay between the consumptions of IC12H26 and the secondary heat release peak observed in Fig. 7. The consumption rates for the same smallest components C_2H_2 and CH_4 are also plotted in Fig. 13. The regions of production (red) and consumption (blue) correspond exactly with **Region II** and **Region III** respectively. Since little fuel evaporation is observed in **Region III**, it corresponds to a premixed prevapourised combustion regime and is not directly affected by the liquid phase. Probability density plot for **Region III** shown in Fig. 14b also validates the lean premixed combustion resulting in the main heat release zone for At-J. However, it can also be noticed that mixture is highly stratified over a wide range of equivalence ratios.

The existing methodologies for detecting flame regimes from detailed experiments and resolved simulations [27] can be used and integrated into the LES framework to capture and model the flame regimes observed for both the fuels.

4. Conclusions

The large-scale realistic configuration LOTAR operated at ONERA was chosen as a simulation test case to understand the mechanism and structures of turbulent multicomponent spray flame. A dynamically thickened flame model integrated with a generic-self-adapting sensor and a discrete multicomponent evaporation model was successfully used compare the combustion behaviour of two fuels: multicomponent surrogate of standard JetA-1 and a sustainable aviation fuel At-J.

Differences in the vapourisation time scales between the two fuels lead to an extended evaporation zone for JetA-1 inside the combustor and a significantly shorter evaporation zone for At-J in the reacting conditions. These changes in the fuel and vapourisation behaviour are associated with corresponding differences in the flame structures. The volatile components for both fuels help in stabilizing the flame by initiating the reactions. Three different regions were identified for both fuels, each associated with different combustion regimes. The evaporation, reaction region of JetA-1 extending into the rich downstream regions of the combustor can indicate the possibility of unburnt hydrocarbons exiting the domain. In case of the At-J bulk of the heat release is associated with premixed combustion of a stratified mixture of pyrolysed fuel components, with negligible influence of the liquid phase.

In summary, the state-of-the art in terms of simulating realistic and alternative jet fuels in practical configurations has been demonstrated. However, the work raises issues about modelling challenges and uncertainties which can affect the discussed results. The highlighted outcomes of the simulations must be compared with additional detailed experimental data, to validate the distribution in the vapour phase due to preferential evaporation. Inclusion of secondary breakup models, film atomisation to better match the droplet profiles will improve confidence of the existing simulation strategy, especially when looking at more realistic operating points where the multi-point injections in the radial swirlers are also utilised. The use of conjugate heat transfer coupled with detailed Lagrangian spray-wall interaction modelling would be especially useful in understanding the flame regimes near the wall, especially for JetA-1. The challenges and immediate need to focus on improving spray flame simulations by developing models to identify multiple regimes and implementing strategies to handle single droplet combustion have also been discussed. The ideas will be explored in the future works.

Acknowledgments

This project has received funding from the European Union's Horizon 2020 research and innovation programme under Agreement 723525 (JETSCREEN) and under the Marie Sklodowska-Curie Grant Agreement 766264 (MAGISTER). The HPC resources from GENCI-TGCC (Grant 2021-A0092B10157) and PRACE (Grant 2019215145 CLEANERFLAMES) are acknowledged. Special thanks to Quentin Cazères and Jonathan Wirtz of CERFACS for the chemistry.

Supplementary material

Chemical_mechanisms.xlsx contains the two chemical mechanisms used and comparisons with the detailed mechanism. **Supplementary_1.pdf** contains additional details of the preferential evaporation across the domain. These are distribution of evaporation source terms, liquid droplet compositions and gaseous mass fractions of the fuel components.

References

[1] M. A. Nemitallah, S. S. Rashwan, I. B. Mansir, A. A. Abdelhafez, M. A. Habib, Review of novel combustion techniques for clean power production in gas turbines, Energy & Fuels 32 (2) (2018) 979–1004.

[2] P. Jenny, D. Roekaerts, N. Beishuizen, Modeling of turbulent dilute spray combustion, Progress in Energy and Combustion Science 38 (6) (2012) 846–887.

[3] K. Luo, H. Pitsch, M. Pai, O. Desjardins, Direct numerical simulations and analysis of three-dimensional n-heptane spray flames in a model swirl combustor, Proceedings of the Combustion Institute 33 (2) (2011) 2143–2152.

[4] L. Ma, D. Roekaerts, Numerical study of the multi-flame structure in spray combustion, Proceedings of the Combustion Institute 36 (2) (2017) 2603–2613.

[5] D. Noh, S. Gallot-Lavallée, W. P. Jones, S. Navarro-Martinez, Comparison of droplet evaporation models for a turbulent, non-swirling jet flame with a polydisperse droplet distribution, Combustion and Flame 194 (2018) 135–151.

[6] D. Paulhiac, B. Cuenot, E. Riber, L. Esclapez, S. Richard, Analysis of the spray flame structure in a lab-scale burner using large eddy simulation and discrete particle simulation, Combustion and Flame 212 (2020) 25–38.

[7] L. Shafer, R. Striebich, J. Gomach, T. Edwards, Chemical class composition of commercial jet fuels and other specialty kerosene fuels, in: 14th AIAA/AHI Space Planes and Hypersonic Systems and Technologies Conference, 2006, p. 7972.

[8] J. Heyne, B. Rauch, P. Le Clercq, M. Colket, Sustainable aviation fuel prescreening tools and procedures, Fuel 290 (2021) 120004.

[9] M. M. Yasin, R. Cant, C. Chong, S. Hochgreb, Discrete multicomponent model for biodiesel spray combustion simulation, Fuel 126 (2014) 44–54.

[10] G. Eckel, J. Grohmann, L. Cantu, N. Slavinskaya, T. Kathrotia, M. Rachner, P. Le Clercq, W. Meier, M. Aigner, Les of a swirl-stabilized kerosene spray flame with a multi-component vaporization model and detailed chemistry, Combustion and Flame 207 (2019) 134–152.

[11] T. Jaravel, Prediction of pollutants in gas turbines using large eddy simulation, Ph.D. thesis, Institut National Polytechnique de Toulouse (2016).

[12] B. Rochette, E. Riber, B. Cuenot, O. Vermorel, A generic and self-adapting method for flame detection and thickening in the thickened flame model, Combustion and Flame 212 (2020) 448–458.

[13] J. M. Apeloig, F.-X. d'Herbigny, F. Simon, P. Gajan, M. Orain, S. Roux, Liquid-fuel behavior in an aeronautical injector submitted to thermoacoustic instabilities, Journal of Propulsion and Power 31 (1) (2015) 309–319.

[14] P. Moin, S. V. Apte, Large-eddy simulation of realistic gas turbine combustors, AIAA journal 44 (4) (2006) 698–708.

[15] CERFACS, AVBP, `http://cerfacs.fr/avbp7x/`, accessed: 2022-07-07.

[16] P. D. Lax, B. Wendroff, Difference schemes for hyperbolic equations with high order of accuracy, Communications on pure and applied mathematics 17 (3) (1964) 381–398.

[17] F. Nicoud, H. B. Toda, O. Cabrit, S. Bose, J. Lee, Using singular values to build a subgrid-scale model for large eddy simulations, Physics of fluids 23 (8) (2011) 085106.

[18] F. Charlette, C. Meneveau, D. Veynante, A power-law flame wrinkling model for LES of premixed turbulent combustion part II: dynamic formulation, Combustion and Flame 131 (1-2) (2002) 181–197.

[19] W. A. Sirignano, Fluid dynamics and transport of droplets and sprays, Cambridge university press, 2010.

[20] A. Felden, L. Esclapez, E. Riber, B. Cuenot, H. Wang, Including real fuel chemistry in LES of turbulent spray combustion, Combustion and Flame 193 (2018) 397–416.

[21] M. Sanjosé, J. Senoner, F. Jaegle, B. Cuenot, S. Moreau, T. Poinsot, Fuel injection model for euler–euler and euler–lagrange large-eddy simulations of an evaporating spray inside an aeronautical combustor, International Journal of Multiphase Flow 37 (5) (2011) 514–529.

[22] T. Schripp, F. Herrmann, P. Oßwald, M. Köhler, A. Zschocke, D. Weigelt, M. Mroch, C. Werner-Spatz, Particle emissions of two unblended alternative jet fuels in a full scale jet engine, Fuel 256 (2019) 115903.

[23] Q. Cazères, P. Pepiot, E. Riber, B. Cuenot, A fully automatic procedure for the analytical reduction of chemical kinetics mechanisms for computational fluid dynamics applications, Fuel 303 (2021) 121247.

[24] M. Stöhr, S. Ruoff, B. Rauch, W. Meier, P. L. Clercq, Droplet vaporization for conventional and alternative jet fuels at realistic temperature conditions: Systematic measurements and numerical modeling, Proceedings of the Combustion Institute 38 (2) (2021) 3269–3276.

[25] V. Shastry, Q. Cazeres, B. Rochette, E. Riber, B. Cuenot, Numerical study of multicomponent spray flame propagation, Proceedings of the Combustion Institute 38 (2) (2020) 3201–3211.

[26] D. Paulhiac, Modélisation de la combustion d'un spray dans un brûleur aéronautique, Ph.D. thesis, Institut National Polytechnique de Toulouse (2015).

[27] S. Hartl, D. Geyer, A. Dreizler, G. Magnotti, R. S. Barlow, C. Hasse, Regime identification from raman/rayleigh line measurements in partially premixed flames, Combustion and Flame 189 (2018) 126–141.